Pure Appl. Chem., Vol. 79, No. 10, pp. 1675–1689, 2007.
doi:10.1351/pac200779101675

A_3B Intermetallics: Defect chemistry and nonstoichiometry*

Herbert Ipser‡

Department of Inorganic Chemistry/Materials Chemistry, University of Vienna, Währingerstrasse 42, A-1090 Vienna, Austria

Abstract: The defect chemistry of different ordered intermetallic compounds with the A_3B stoichiometry was investigated. Three groups were distinguished according to their crystal structure: $L1_2$ compounds (Ni_3Al, Ni_3Ga, Pt_3Ga, Pt_3In), $D0_{19}$ compounds (Ti_3Al), and $D0_3$ compounds (Fe_3Al, Ni_3Sb). Statistical–thermodynamic models were derived based on a Wagner–Schottky approach, and the calculated activity curves (thermodynamic activity vs. composition) were compared with experimental activity data. In this way, we attempted to obtain at least estimated values for the energies of formation of the different types of point defects present in the corresponding compound, both as configurational defects (which are responsible for nonstoichiometry) and as thermal defects. In the majority of cases, thermodynamic activities had to be determined experimentally in the present study, using either an emf method with a solid electrolyte (Ni_3Ga, Pt_3Ga, Pt_3In, Fe_3Al) or a Knudsen cell-mass spectrometric method (Ni_3Sb).

Keywords: intermetallics; A_3B intermetallics; Wagner–Schottky; configurational defects; thermal defects; nonstoichiometry.

INTRODUCTION

Ni-based superalloys are a group of metallic materials that are of considerable technological interest. Generally, they are based on different intermetallic compounds of Ni, but many of them consist of a combination of γ (disordered fcc (Ni)-phase) and γ' (ordered $L1_2$-type Ni_3Al phase) [1]. They are used, for example, in turbines due to their excellent high-temperature mechanical and corrosive properties, but they are also used for many other structural applications. Coherent precipitates of the ordered $L1_2$ Ni_3Al phase are one key component, and the particular properties of this intermetallic compound are certainly influenced also by its structure on the atomic level (i.e., by its degree of order in the crystal lattice, which changes with temperature). It seems to be clear that nonstoichiometry in this compound is mainly caused by antistructure atoms (atoms on "wrong" lattice sites) and that the thermal disorder is based on the same type of point defects. Many more intermetallic A_3B compounds crystallize in the cubic $L1_2$ structure, however, most of them are of negligible technological interest, mainly due to weight and price considerations. Nevertheless, it may still be of interest to learn more about the general mechanism of nonstoichiometry in all these compounds and to compare their ordering properties.

There are many more intermetallic A_3B compounds of interest with different crystal structures (for a general overview, see refs. [2,3]), among them nonstoichiometric compounds based on the hexagonal $D0_{19}$-type structure (as, e.g., Ti_3Al) or those based on the cubic $D0_3$-type structure (as, e.g.,

*Paper based on a presentation at the 12th International IUPAC Conference on High Temperature Materials Chemistry (HTMC-XII), 18–22 September 2006, Vienna, Austria. Other presentations are published in this issue, pp. 1635–1778.

‡E-mail: herbert.ipser@univie.ac.at

Fe_3Al). In all cases, various types of point defects are responsible both for nonstoichiometry as well as for thermal disorder. It is clear that the type and the concentration of the point defects that are present in the crystal lattice will be responsible for many of the properties of these compounds.

Although different experimental and theoretical methods are available to determine defect concentrations in such compounds, each of them has its shortcomings and may break down under certain circumstances. It has been shown for different types of intermetallics (see, e.g., refs. [4–9]) that the combination of accurate thermodynamic measurements with appropriate statistical–thermodynamic models can be a very powerful tool to determine the types of point defects present in a nonstoichiometric intermetallic compound and the variation of their concentrations with composition and temperature. In addition, it provides a possibility to, at least, estimate values for the corresponding energies of formation of the different point defects.

Thus, it will be shown for intermetallic compounds with $L1_2$, $D0_{19}$, and $D0_3$ structure how an appropriate statistical–thermodynamic model can be used to evaluate experimental results of thermodynamic activities and to derive information on type and concentration of point defects in the different compounds.

TYPES OF INTERMETALLIC COMPOUNDS

Intermetallics with the $L1_2$ structure

As mentioned above, Ni_3Al is one of the prominent examples crystallizing in the cubic $L1_2$ structure. The most recent version of the Ni–Al phase diagram can be found in refs. [10,11], and it seems to be clear now that the eutectic reaction takes place between γ'-Ni_3Al and B2-NiAl (and not between γ'-Ni_3Al and γ-(Ni) as shown, for example, in the diagram in Massalski et al. [12]). The ideal (i.e., perfectly ordered) $L1_2$ crystal structure itself is shown in Fig. 1; it can be derived from the cubic fcc structure, if all corner positions of the unit cell (the β-sublattice) are occupied by B atoms and all face-centered positions (the α-sublattice) by A atoms, yielding automatically the A_3B stoichiometry.

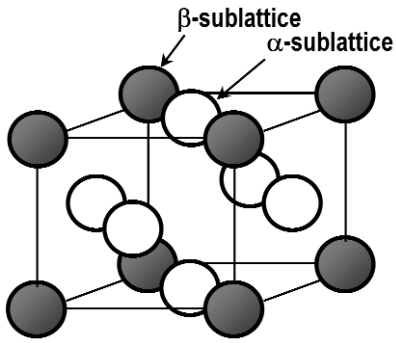

Fig. 1 $L1_2$-type crystal structure.

In addition to Ni_3Al, a number of other intermetallics with this crystal structure were investigated in the present study (i.e., Ni_3Ga, Pt_3Ga, and Pt_3In).

Intermetallics with the $D0_{19}$ structure

The most prominent example of intermetallics with the hexagonal $D0_{19}$ structure is probably Ti_3Al. There has been considerable confusion in the literature about the exact phase relationships between α-(Ti), β-(Ti), and Ti_3Al [13–19], but it appears that this question has been settled now: Ti_3Al trans-

forms with a congruent temperature maximum first into α-(Ti) which itself transforms into β-(Ti) at a slightly higher temperature, however, there is no direct transition between Ti_3Al and β-(Ti) [19]. The crystal structure itself is shown in Fig. 2. It can be derived from the hcp structure by a regular arrangement of A and B atoms in the hcp layers in a corresponding 3:1 ratio, and this relationship with the hcp lattice is indicated by bold lines in the figure.

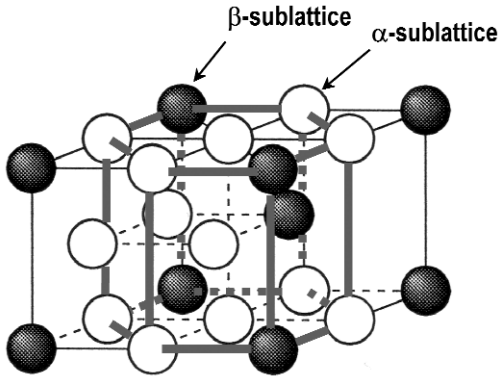

Fig. 2 $D0_{19}$-type crystal structure; the bold lines indicate the relationship with the hcp crystal structure (see text).

Intermetallics with the $D0_3$ structure

Here, it is the compound Fe_3Al, which is probably the most prominent representative of intermetallics with this structure type. Fe_3Al is a low-temperature phase which transforms around 550 °C into B2-FeAl, which itself transforms at higher temperatures into bcc (αFe) [12]. The crystal structure is shown in a primitive cubic setting in Fig. 3. (It should be mentioned that it is sometimes also represented in an fcc setting of the unit cell.) This structure type can be derived from the bcc structure: if one combines eight bcc unit cells to a larger cube, and if the body-centered positions are occupied alternately by A and B atoms whereas the corner positions are all occupied by A atoms, then one arrives at perfectly ordered A_3B in the $D0_3$-type.

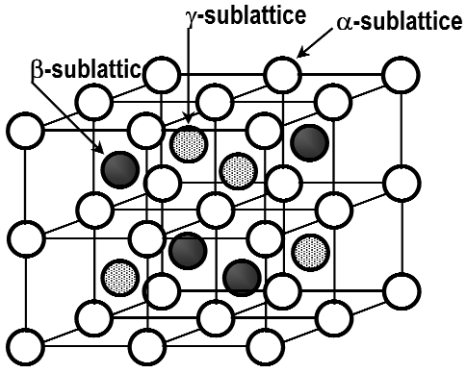

Fig. 3 $D0_3$-type crystal structure (primitive cubic setting).

One more intermetallic with this crystal structure was investigate in this study, namely, Ni_3Sb, which is a typical high-temperature phase [12,20] stable between about 530 and 1160 °C. As will be

discussed below, the defect mechanism responsible for nonstoichiometry in Ni_3Sb seems to be completely different from that for Fe_3Al.

STATISTICAL THERMODYNAMIC MODELS

Types of models

Various statistical–thermodynamic approaches have been developed in the literature to describe ordered intermetallic compounds. One can distinguish three basic types of models, namely,

- the Bragg–Williams approach [21,22],
- the Wagner–Schottky approach [23], and
- the quasi-chemical approach (see, e.g., [24]).

In the present case, the Wagner–Schottky approach was used (for more information on the other types of models, the reader is referred to the corresponding references). It is based on the assumption that the Gibbs energy of the real crystal (which contains various types of defects) can be calculated as

$$G = G^0 + \sum n_{\text{defect}} \times G_{\text{defect}} - T \times S_{\text{conf}} \tag{1}$$

where G^0 is the Gibbs energy of the perfectly ordered crystal, G_{defect} is the Gibbs energy contribution of a particular type of point defect (vacancy, antistructure atom, interstitial atom), n_{defect} is the corresponding number of defects, and S_{conf} is the configurational entropy. The defects are assumed to be non-interacting, and very frequently G_{defect} is approximated by the contribution to the internal energy, U_{defect}, neglecting all influences by the point defects on the vibrational entropy and the volume of the crystal. The configurational entropy is usually calculated by the well-known Boltzmann equation

$$S_{\text{conf}} = k \times \ln W \tag{2}$$

At the end, the Gibbs energy has to be minimized to find its value for the real crystal in the thermodynamically stable state.

Derivation of the model for $L1_2$ compounds

All details of the derivation of the statistical–thermodynamic model for $L1_2$ phases can be found in the paper by Krachler et al. [25]. According to Fig. 1, the crystal lattice is divided into two sublattices, the α- and the β-sublattice, where, in the fully ordered crystal, the α-sublattice is occupied by A-atoms and the β-sublattice by B-atoms only. From the figure, it can also be seen that the coordination number of B-atoms (on the β-sublattice) is 12 (i.e., each B-atom is surrounded by 12 A-atoms), whereas the coordination number of A-atoms is 4 + 8 (i.e., each A atom on the α-sublattice has 4 B- and 8 A-atoms as nearest neighbors). If N^1 is the total number of lattice sites, then there are $N^\alpha = ¾\, N^1$ α-sublattice sites and $N^\beta = ¼\, N^1$ β-sublattice sites. Four types of point defects are allowed, vacancies and antistructure atoms on both sublattices, and their numbers are N_V^α, N_V^β, N_A^β, and N_B^α. Usually, interstitial defects do not play any significant role in intermetallic compounds of the type considered here and are therefore entirely neglected.

A so-called grand-canonical approach is used for the derivation, which means that one has an open system (both energy and mass can be exchanged with the surrounding), and the crystal is assumed to have a constant volume, corresponding to a constant number of lattice sites, N^1. In such a case, one has to use the grand partition function Ξ

$$\Xi = \sum_n \exp\left[\left(\mu_A \frac{(N_A)_n}{N_L} + \mu_B \frac{(N_B)_n}{N_L} - E_n\right) / kT\right] \tag{3}$$

where μ_A and μ_B are the chemical potentials of the two components A and B, $(N_A)_n$ and $(N_B)_n$ are the numbers of A- and B-atoms, and E_n is the total energy of the system when it is in the state n. The corresponding thermodynamic potential is the grand potential Ω

$$\Omega = -kT \ln \Xi \tag{4}$$

After minimization of the grand potential Ω, one can calculate the chemical potentials (thermodynamic activities) and the defect concentrations as functions of temperature and composition, and as function of the corresponding parameters. In the present case, the defect formation energies $E_f(B^\alpha)$, $E_f(A^\beta)$, $E_f(V^\alpha)$, and $E_f(V^\beta)$ were used as adjustable parameters, where $E_f(B^\alpha)$ is the energy necessary to create an antistructure B-atom on the α-sublattice, and so on. These parameters may be determined or, at least, estimated by a curve fitting procedure based on experimental data for thermodynamic activities or defect concentrations.

Application of the $L1_2$ model to Ni_3Al

Altogether six different sets of defect formation energies, $E_f(Al^{Ni})$, $E_f(Ni^{Al})$, $E_f(V^{Ni})$, and $E_f(V^{Al})$, were originally found in the literature for the compound Ni_3Al [26–31], which are listed in the first six rows of Table 1. They had been obtained by different theoretical methods. These defect formation energies were used as parameters to calculate aluminum activities as a function of composition at 1400 K, based on the statistical model approach outlined above, and the corresponding curves were compared with experimental activity data by Steiner and Komarek [33]. As can be seen from Fig. 4, the curve which is based on the defect formation energies by Debiaggi et al. [26] gives the best agreement with the experimental data, and this was supported by a second, independent set of experimental activity data by Hilpert et al. [34] at 1600 K (cf. Fig. 3 in ref. [25]). This apparently suggests that the energy parameters by Debiaggi et al. [26] should be the most reliable of all. Using these parameters, the concentrations of the four different types of point defects were calculated as functions of the composition within Ni_3Al; the corresponding result is shown in Fig. 5. It can be seen that the deviation from stoichiometry is practically entirely caused by antistructure atoms on the two sublattices, whereas vacancies play a negligible role: their concentrations are so small that the corresponding curves virtually coincide with the axis in Fig. 5. This is also reflected by the much higher values of the defect formation energies for vacancies than for antistructure atoms as obtained by all of the authors [26–32] (cf. Table 1).

Table 1 Ni_3Al: Defect formation energies from various theoretical approaches.

$E_f(B^\alpha)$	$E_f(A^\beta)$	$E_f(V^\alpha)$	$E_f(V^\beta)$	Ref.
0.31	0.66	1.48	2.14	Debiaggi et al. [26]
0.31	1.02	1.42	1.65	Gao et al. [27]
0.58	0.54	1.47	1.91	Foiles and Daw [28]
0.69	0.75	1.87	2.65	Fu and Painter [29]
0.59	0.56	1.47	1.92	Sun and Lin [30]
0.53	0.62	1.51	2.02	Schweiger et al. [31]
0.51	0.51	1.50	2.00	Schweiger et al. [32]

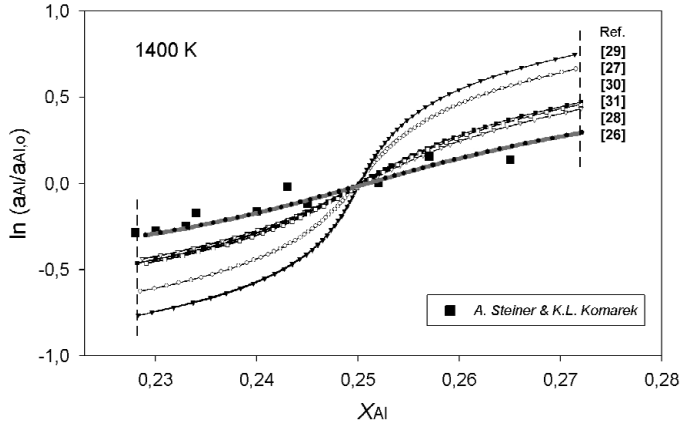

Fig. 4 Ni_3Al: Comparison of calculated activity curves (see text) with experimental results for the thermodynamic activity of Al at 1400 K by Steiner and Komarek [33].

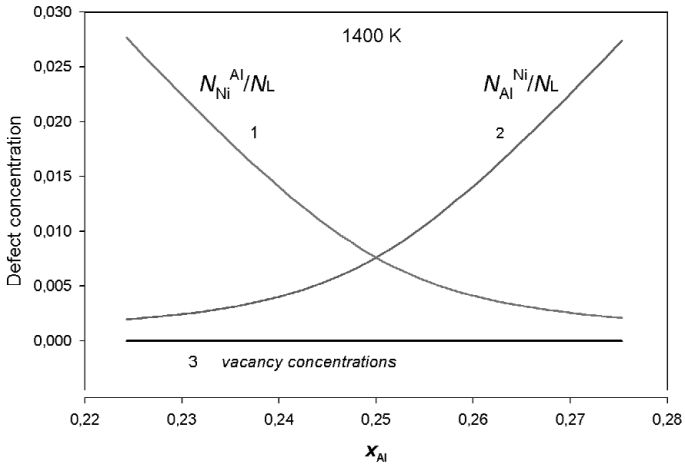

Fig. 5 Ni_3Al: Defect concentrations as a function of composition at 1400 K calculated with the defect formation energies by Debiaggi et al. [26]; (1) concentration of Ni antistructure atoms; (2) concentration of Al antistructure atoms; (3) concentration of Ni vacancies coinciding here with the curve for the Al vacancies.

In the following, several theoretical approaches were tested by Schweiger et al. [32] to find out which of them would result in the most reliable set of defect formation energies when compared with experimental activity data. Using the VASP software [35,36], it was found that a generalized gradient approximation (GGA) considering structural relaxation effects gave the best results as listed in the last row of Table 1. It is interesting to note that the average value of the formation energies of antistructure defects by Debiaggi et al. [26] is in excellent agreement with the values by Schweiger et al. [32], which came out to be equal.

Application of the $L1_2$ model to Ni_3Ga, Pt_3Ga, and Pt_3In

In order to test the applicability of the model to other $L1_2$ compounds, experimental emf measurements were performed in the three compounds Ni_3Ga, Pt_3Ga, and Pt_3In to obtain thermodynamic activities of Ga or In, respectively. All details of the experimental method have been described in detail by Yuan et al. [37]; it is based on a galvanic cell using stabilized zirconia as a solid oxygen-conducting electrolyte

(–) Ni_3Ga, Ga_2O_3 | ZrO_2 (stab.) | Fe, Fe_xO (+) (5)

The emf of this cell can be combined with literature values [38] for the cell

(–) Ga, Ga_2O_3 | ZrO_2 (stab.) | Fe, Fe_xO (+) (6)

to give the emf of the hypothetical cell

(–) Ga, Ga_2O_3 | ZrO_2 (stabilized by CaO or Y_2O_3) | Ni_3Ga, Ga_2O_3 (+) (7)

(For practical purposes, the cell type 5 was preferred over type 7 since pure Ga is liquid at the temperatures of the experiments.) From the emf of cell 7, the thermodynamic activity of gallium can be calculated according to eq. 8

$$\Delta\bar{G}_{Ga} = \bar{G}_{Ga} - G^{o}_{Ga} = -zEF = RT \ln a_{Ga} \quad (8)$$

where F is the Faraday constant, E is the measured emf value in V, and z is the number of electrons exchanged (which is 3 in the current case). Figure 6 shows the corresponding results for a temperature of 1123 K.

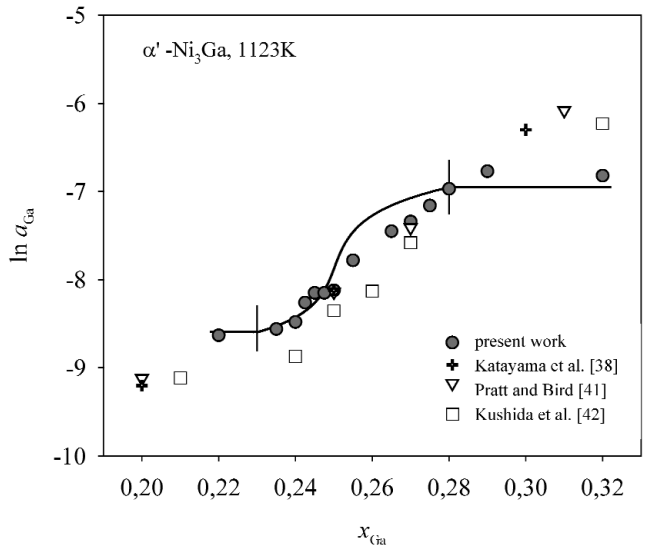

Fig. 6 Ni_3Ga: Experimental values of the Ga activity at 1123 K as a function of composition; the full line within the homogeneity range of the phase was calculated with the statistical–thermodynamic model, using the following defect formation energies: $E_f(Ni^{Ga}) = E_f(Ga^{Ni}) = 0.6$ eV, $E_f(V^{Ni}) = 1.5$ eV, $E_f(V^{Ga}) = 2.0$ eV.

Since no defect formation energies were available in the literature for Ni_3Ga, they were estimated by fitting a statistical–theoretical activity curve to the obtained experimental values. The full curve through the data points within the homogeneity range of Ni_3Ga was calculated with the following defect formation energies [37]

$E_f(Ni^{Ga}) = 0.60$ eV, $E_f(Ga^{Ni}) = 0.60$ eV, $E_f(V^{Ni}) = 1.5$ eV, $E_f(V^{Ga}) = 2.0$ eV

These values, with energies of formation much larger for vacancies than for antistructure atoms, correspond again to a defect mechanism based on antistructure atoms (i.e., the nonstoichiometry of Ni_3Ga is caused by antistructure atoms whereas vacancies play a negligible role).

Similar experiments were performed for Pt_3Ga [39] and Pt_3In [40], and the defect formation energies were determined by a corresponding statistical–thermodynamic evaluation of the obtained activity values.

Table 2 lists the defect formation energies of all $L1_2$ compounds investigated in our laboratory. In all cases, the energies of formation of the vacancies were assumed to be higher than those of the antistructure atoms, following the results of the ab initio calculations for Ni_3Al [26–32]. The energies of formation of the antistructure atoms increase from Ni_3Al over Ni_3Ga, Pt_3In to Pt_3Ga, which indicates clearly an increasing ordering tendency in these compounds in the same sequence, as higher defect formation energies correspond to smaller defect concentrations.

Table 2 Defect formation energies for various intermetallic $L1_2$ compounds.

$E_f(A^B)$	$E_f(B^A)$	$E_f(V^A)$	$E_f(V^B)$	Intermetallic compound	Ref.
	eV				
0.31	0.66	1.48	2.14	Ni_3Al	Debiaggi et al. [26]
0.51	0.51	1.50	2.00	Ni_3Al	Schweiger et al. [32]
0.60	0.60	1.50	2.00	Ni_3Ga	Yuan et al. [37]
1.25	1.25	2.00	2.00	Pt_3Ga	Schweitzer et al. [39]
1.15	1.15	2.00	2.00	Pt_3In	Schweitzer et al. [40]

Derivation of the model for $D0_{19}$ compounds and application to Ti_3Al

As outlined above, the hexagonal $D0_{19}$ structure can be derived from the hcp A3 structure by a regular ordering of the two types of atoms A and B. Analogous to the case of the $L1_2$ structure, the crystal lattice is divided into two sublattices for the statistical–thermodynamic calculations, the α- and the β-sublattice, and the number of sublattice sites is given by $N^\alpha = \frac{3}{4} N^l$ and $N^\beta = \frac{1}{4} N^l$ (cf. Fig. 2). From this figure, it can also be seen that the coordination numbers of the two types of atoms are the same as in the case of $L1_2$: each A-atom on the α-sublattice is surrounded by 8 A-atoms and 4 B-atoms, whereas each B-atom has 12 A-atoms as nearest neighbors. This means, that from a statistical–thermodynamic point of view, the two crystal structures are analogous and can be treated with the same formalism. Consequently, the model equations for $L1_2$ phases that were derived by Krachler et al. [25] can be likewise applied to compounds crystallizing in the $D0_{19}$ structure. All other details can be found in ref. [43].

Thermodynamic activities of Al in the composition range of Ti_3Al were determined experimentally by Samokhval et al. [44] and Reddy et al. [45] (emf method with CaF_2 as solid electrolyte, about 820 to 1010 K), and by Eckert et al. [46] (Knudsen cell-mass spectrometric method, about 1180 to 1430 K). In order to be able to compare the corresponding experimental data, an average temperature of 1123 K was chosen and all activity values were converted to this temperature. Unfortunately, the absolute activity values were in severe disagreement, which was most probably due to the different temperature ranges of the experiments and the errors incurred by converting them to a common temperature of 1123 K. However, if the data sets were normalized with respect to the activity at the exactly stoichiometric composition (i.e., if values of $a_{Al}/a_{Al,0}$ were calculated), the data became more or less consistent. The resulting activity values are shown in Fig. 7.

Based on experimental evidence from refs. [47–51] it was assumed for the calculation of the theoretical activity curves in Fig. 7 that the energies of formation of vacancies on the two sublattices would be rather high compared to those for antistructure atoms. From their positron annihilation study, Würschum et al. derived a value for the vacancy formation enthalpy of 1.55 ± 0.2 eV [47]. Therefore, it was assumed that $E_f(V^\alpha) = E_f(V^\beta) = 1.5$ eV would be a reasonable value for the vacancy formation energies in our calculations. All the corresponding arguments are discussed in detail in ref. [43].

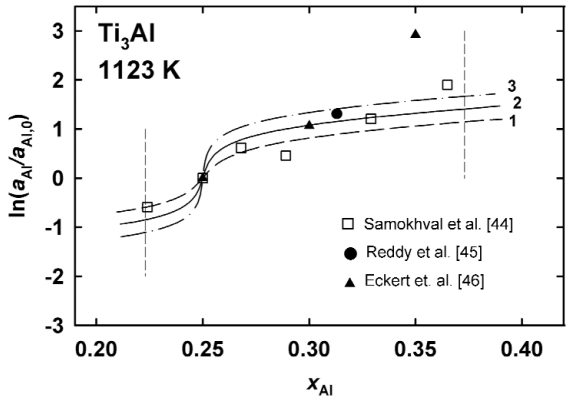

Fig. 7 Ti_3Al: Experimental values of the Al activity at 1123 K as a function of composition; the three lines were calculated with the statistical–thermodynamic model using the following defect formation energies: $E_f(V^{Ti}) = E_f(V^{Al}) = 1.5$ eV; $E_f(Ti^{Al}) = E_f(Al^{Ti}) = 0.5$ eV (curve 1), $E_f(Ti^{Al}) = E_f(Al^{Ti}) = 0.6$ eV (curve 2), $E_f(Ti^{Al}) = E_f(Al^{Ti}) = 0.7$ eV (curve 3).

In Fig. 7, three theoretical curves are drawn through the experimental activity data at 1123 K using the following parameter sets

$E_f(V^\alpha) = E_f(V^\beta) = 1.5$ eV; $E_f(A^\beta) = E_f(B^\alpha) = 0.5$ eV (curve 1)

$E_f(V^\alpha) = E_f(V^\beta) = 1.5$ eV; $E_f(A^\beta) = E_f(B^\alpha) = 0.6$ eV (curve 2)

$E_f(V^\alpha) = E_f(V^\beta) = 1.5$ eV; $E_f(A^\beta) = E_f(B^\alpha) = 0.7$ eV (curve 3)

Although the scatter of the data points is considerable, it is probably safe to conclude that the energies of formation of antistructure defects should lie within the indicated range (i.e., between 0.5 and 0.7 eV). There is only one single data point at 35 atom % Al by Eckert et al. [44] with a large deviation. However, one has to keep in mind that the simplifying assumptions of the statistical–thermodynamic model become increasingly less valid with large deviations from stoichiometry where the defect concentrations become large and the defects are certainly not isolated anymore. Therefore, a value of $E_f(A^\beta) = E_f(B^\alpha) = 0.6 \pm 0.1$ eV is suggested for the energies of formation of antistructure atoms.

Derivation of the model for $D0_3$ compounds

Different from the previous cases, the crystal lattice of a fully ordered stoichiometric compound A_3B with the cubic $D0_3$ superstructure can be divided into three different sublattices, α, β, and γ, where A-atoms occupy the α- and γ-positions and B-atoms the β-positions (cf. Fig. 3). If N^l is the total number of lattice sites, then the numbers of sublattice sites are given by

$N^\alpha = N^l/2$, $N^\beta = N^l/4$, $N^\gamma = N^l/4$

Six types of point defects are allowed in the lattice, and these are antistructure atoms and vacancies on the three sublattices; their numbers are given by N_A^β, N_B^α, N_B^γ, N_V^α, N_V^β, N_V^γ. As a consequence, there are also six different defect formation energies that can be used as variable parameters in the model calculations, namely, $E_f(A^\beta)$, $E_f(B^\alpha)$, $E_f(B^\gamma)$, $E_f(V^\alpha)$, $E_f(V^\beta)$, and $E_f(V^\gamma)$, where $E_f(A^\beta)$ is the energy of formation of an antistructure A-atom on the β-sublattice, with all other definitions correspondingly. All details of the derivation of the model equations can be found in ref. [52].

Application of the $D0_3$ model to Fe_3Al

The intermetallic compound Fe_3Al crystallizes in the $D0_3$ structure at temperatures below 552 °C where it transforms into the B2 structure [53]. This means that above the transition temperature the β- and the γ-sublattice become completely disordered with a random distribution of Fe and Al atoms on both of them. This is apparently a consequence of very low energies necessary to form antistructure defects on these two sublattices, which is in perfect agreement with the effective defect formation energies at $x_{Al} = 0.25$ as obtained by ab initio calculations by Fähnle et al. [54] (see Table 3). The α-sublattice remains more or less ordered (i.e., occupied mainly by Fe atoms), which is in line with the much higher value of $E_f(Al^{\alpha})$. Only at temperatures around 800 °C occurs another transformation from the B2- into the A2-type, which results in a complete disorder (i.e., a completely random distribution of Fe and Al atoms over all three sublattices). According to the high values of the effective vacancy formation energies in Fe_3Al, vacancies do not play any significant role within the stability range of the $D0_3$ structure, that is, their compositions are much lower than those of antistructure defects on the β- and the γ-sublattice.

Table 3 Effective defect formation energies at the stoichiometric composition (x_{Al}, $x_{Sb} = 0.25$) in the $D0_3$ compounds Fe_3Al and Ni_3Sb obtained from ab initio calculations.

Compound	Defect formation energies (in eV)						Ref.	
	$E_f(Fe^{\beta})$	$E_f(Al^{\alpha})$	$E_f(Al^{\gamma})$	$E_f(V^{\alpha})$	$E_f(V^{\beta})$	$E_f(V^{\gamma})$		
Fe_3Al	0.05	1.79	0.05	1.18	1.53	2.45	[54]	
	$E_f(Ni^{\beta})$	$E_f(Sb^{\alpha})$	$E_f(Sb^{\gamma})$	$E_f(V^{\alpha})$	$E_f(V^{\beta})$	$E_f(V^{\gamma})$		
Ni_3Sb	0.22	4.47	3.20	0.21	1.99	0.44	[64]	structural relaxation only
	0.25	4.13	2.98	0.25	1.86	0.49	[66]	structural and volume relaxation

Since no experimental thermodynamic data for the corresponding temperature and composition range were available in the literature, the following solid-state galvanic cell was used by Huang et al. [55] for the determination of the partial thermodynamic properties of the $D0_3$-phase Fe_3Al as a function of temperature and composition

$$(-)\ Pt \mid Ir \mid Al_{0.85}Sn_{0.15},\ Na_3AlF_6 \mid CaF_2 \mid Al_{1\pm x}Fe_{3\pm x},\ Na_3AlF_6 \mid Ir \mid Pt\ (+) \tag{9}$$

The virtual reactions in the left- and right-hand side electrode are, respectively

$$Al_{(Al–Sn)} + 3\ Na^+ + 6F^- - 3e^- = Na_3AlF_6 \qquad \text{(left)} \tag{10}$$

$$Na_3AlF_6 + 3e^- = Al_{(Al–Fe)} + 3\ Na^+ + 6F^- \qquad \text{(right)} \tag{11}$$

which results in a total cell reaction

$$Al_{(Al–Sn)} = Al_{(Al–Fe)} \tag{12}$$

Hence, the measured emf values of the cell are given by

$$E = -(RT/3F)\ln\frac{a_{Al(Al-Fe)}}{a_{Al(Al-Sn)}} \tag{13}$$

where $a_{Al(Al–Fe)}$ and $a_{Al(Al–Sn)}$ are the thermodynamic activities of Al in Fe_3Al and in the reference Al–Sn alloy. In order to achieve thermodynamic equilibrium within reasonable periods of time, an Al-rich Al–Sn alloy (15 atom % Sn) was selected as a reference electrode. This composition is charac-

terized by a two-phase field between practically pure solid Al and a Sn-rich liquid in the temperature range from 774 K (eutectic temperature) to about 873 K [56]. Thus, by definition, the activity of Al is unity in the reference electrode, and eq. 13 reduces to

$$E = -(RT/3F) \ln a_{\mathrm{Al(Al-Fe)}} \tag{14}$$

As usual, all partial thermodynamic properties of aluminum could be obtained from the emf and its temperature dependence. Figure 8 shows the experimental activities of Al at 750 K in Fe_3Al and the neighboring phase fields as a function of composition.

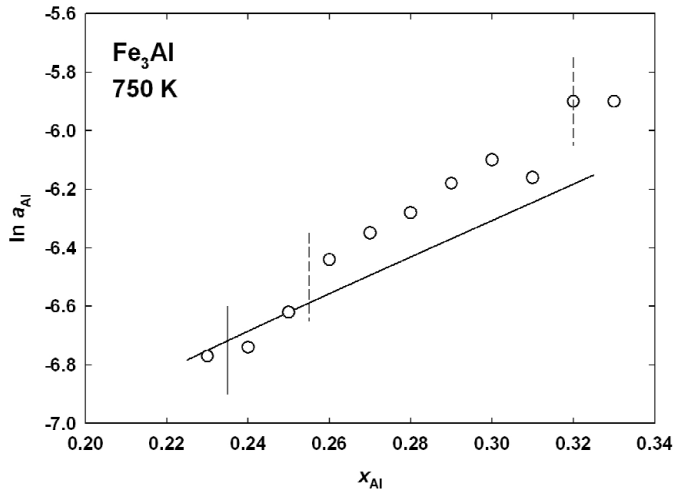

Fig. 8 Fe_3Al: Comparison of statistical–thermodynamic activity curve with experimental data points; the curve was calculated with the defect formation energies from Fähnle and coworkers [54] based on ab initio calculations with structural relaxation only; the vertical dashed lines indicate the phase boundaries according to Ikeda et al. [67], the vertical full line indicates the phase boundary suggested from the present investigation.

Energy changes for the introduction of point defects in the intermetallic compound Fe_3Al had been calculated by Fähnle et al. by means of an ab initio method [54]. Neglecting any changes of the vibrational entropy and the volume in the lattice, and with some simplifications, the effective defect formation energies were derived and are listed in Table 3. Based on the obtained energy values, the variation of ln a_{Al} with composition could be computed, and the result is shown in Fig. 8 together with the experimental data points. It can be seen that the experimental data show a more pronounced increase of ln a_{Al} with rising aluminum content than predicted by these model calculations. The observed discrepancy is most probably due to the neglect of the changes in the vibrational entropy and the volume, as well as to the omission of any influences of the magnetism. Under these circumstances, the agreement is considered very satisfactory.

Application of the $D0_3$ model to Ni_3Sb

Ni_3Sb is a high-temperature phase which is stable between about 530 °C and its congruent melting point around 1160 °C and between about x_{Sb} = 0.25 and 0.29 [12,57]. After some confusion in the literature concerning its actual crystal structure, it was shown by Heinrich et al. [58] that Ni_3Sb crystallizes in the ordered cubic $D0_3$-type structure, and this was confirmed beyond doubt by Randl et al. [59] on the basis of powder neutron diffraction experiments between 600 and 1000 °C.

From a series of investigations, it became obvious that Ni_3Sb exhibits a very high diffusivity: the nickel atoms in this compound show actually the highest mobility ever observed in a metallic system [60–63]. This suggests that the concentration of vacancies must be rather high in this compound. Evidence for a high number of structural vacancies came for the first time from density measurements by Heumann and Stüer [60]. This was confirmed by the extensive neutron diffraction study of Randl et al. [59] who concluded that the nonstoichiometric deviation, which occurs only to the Sb-rich side, is entirely caused by Ni vacancies. A high concentration of Ni vacancies was also supported by an ab initio study by Fähnle and coworkers [64,65] who calculated the effective formation energies for the different types of point defects in Ni_3Sb. The lowest values were obtained for vacancies on the two Ni sublattices and for Ni antistructure atoms (see Table 3). As a consequence, very high concentrations of Ni vacancies were predicted from these calculations, which means that they would be responsible for the nonstoichiometry of Ni_3Sb to the Sb-rich side.

Since again no thermodynamic data for Ni_3Sb were available in the literature, a Knudsen cell mass spectrometric method was employed to determine Sb activities within the homogeneity range of Ni_3Sb and the neighboring two-phase fields. All details of these measurements were described by Popovic et al. [66]. The experimental results (i.e., Sb activities as a function of composition at 1223 K) are shown in Fig. 9.

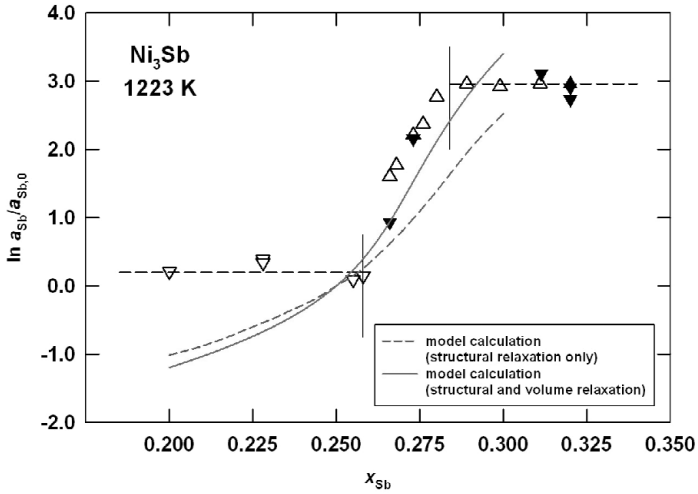

Fig. 9 Ni_3Sb: Comparison of statistical–thermodynamic activity curve with experimental data points; the dashed curve was calculated with the defect formation energies from Fähnle and coworkers [64,65] based on ab initio calculations with structural relaxation only; for the full curve, a volume relaxation was included in the ab initio calculations (cf. Table 3).

For the intermetallic compound Ni_3Sb energy changes for the introduction of point defects had been calculated by Fähnle and coworkers by means of an ab initio method (supercell with 32 lattice sites) [64,65]. Again neglecting any changes of the vibrational entropy and the volume in the lattice, and with some simplifications, the effective defect formation energies were derived which are shown in Table 3. Based on the obtained energy values, the variation of ln a_{Sb} with composition could be computed, and the result is shown in Fig. 9 (dashed line) together with the experimental data points. It can be seen that the experimental data show a more pronounced increase of ln a_{Sb} with rising Sb content than predicted by these model calculations.

In a next step it was attempted to refine the ab initio calculations by allowing a full volume relaxation in the supercell, which resulted in somewhat different energy parameters. The corresponding

effective defect formation energies are included in Table 3. Based on this new calculation, a steeper curve ln a_{Sb} vs. composition was obtained, which describes the experimental activity data considerably better although a small difference can still be observed (cf. full curve in Fig. 9). This small difference may be partly caused by the uncertainty of the activity value at the exactly stoichiometric composition $x_{Sb} = 0.25$ (which had to be estimated since it is not included in the homogeneity range of the compound), but it may also be partially due to the neglect of all influences of the point defects on the vibrational entropy of the crystal in the model calculations (for a detailed discussion, see ref. [66]).

All these results indicate that the defect mechanism in Ni_3Sb is very much different from that of Fe_3Al. Whereas in the latter compound it is substitution (i.e., antistructure defects on the β- and γ-sublattices) that is responsible for nonstoichiometry and thermal disorder, Ni_3Sb exhibits a mixed defect mechanism: the main defects are vacancies on the Ni positions (α- and γ-sublattice) and antistructure atoms on the Sb positions (β-sublattice). However, due to the range of homogeneity (which is shifted entirely to the Sb-rich side, 25.8 to 28.4 atom % Sb) only Ni vacancies are important for the nonstoichiometry.

ACKNOWLEDGMENTS

The author wants to thank W. Yuan, Y. Huang, X. Wu, Z.-Y. Qiao (Beijing, China), J. Dischinger, H.-J. Schaller (Kiel, Germany), A. Schweitzer, and F. Gehringer (Vienna, Austria) for experimental help with the emf measurements as well as A. Popovic (Ljubljana, Slovenia) for the Knudsen cell mass spectrometric measurements; help with the statistical–thermodynamic calculations by O. Semenova and R. Krachler (Vienna, Austria) is also gratefully acknowledged. Financial support of these studies was provided by the Austrian Science Foundation (FWF, Project nos. P12962 and P14519), by the National Natural Science Foundation of China (NSFC), as well as by the Scientific-Technical Cooperation Austria-China.

REFERENCES

1. D. Letzig, J. Klöwer, G. Sauthoff. *Z. Metallkd.* **90**, 712 (1999).
2. G. Sauthoff. *Intermetallics*, VCH, Weinheim (1995).
3. G. Sauthoff. *Intermetallics* **8**, 1101 (2000).
4. (a) R. Krachler, H. Ipser, K. L. Komarek. *J. Phys. Chem. Solids* **50**, 1127 (1989); (b) R. Krachler, H. Ipser, K. L. Komarek. *J. Phys. Chem. Solids* **51**, 1239 (1990).
5. H. Ipser, R. Krachler, G. Hanninger, K. L. Komarek. *High Temp. Chem.* **26**, 345 (1990).
6. R. Krachler, H. Ipser, B. Sepiol, G. Vogl. *Intermetallics* **3**, 83 (1995).
7. J. P. Neumann, Y. A. Chang, C. M. Lee. *Acta Metall.* **24**, 593 (1976).
8. J. P. Neumann, Y. A. Chang. *Z. Metallkd.* **70**, 118 (1979).
9. Y. A. Chang, J. P. Neumann. *Prog. Solid State Chem.* **14**, 221 (1982).
10. N. Dupin, I. Ansara, B. Sundman. *Calphad* **25**, 279 (2001).
11. L. Eleno, K. Frisk, A. Schneider. *Intermetallics* **14**, 1276 (2006).
12. T. B. Massalski, H. Okamoto, P. R. Subramanian, L. Kacprzak (Eds.). *Binary Alloy Phase Diagrams*, 2nd ed., ASM International, Materials Park, OH (1990).
13. U. R. Kattner, J.-C. Lin, Y. A. Chang. *Metall. Trans. A* **23**, 2081 (1992).
14. R. Kainuma, M. Palm, G. Inden. *Intermetallics* **2**, 321 (1994).
15. R. Kainuma, G. Inden. *Z. Metallkd.* **88**, 429 (1997).
16. F. Zhang, S. L. Chen, Y. A. Chang, U. R. Kattner. *Intermetallics* **5**, 471 (1997).
17. H. M. Flower, J. Christodoulou. *Mater. Sci. Technol.* **15**, 45 (1999).
18. I. Ohnuma, Y. Fujita, H. Mitsui, K. Ishikawa, R. Kainuma, K. Ishida. *Acta Mater.* **48**, 3113 (2000).
19. A. Suzuki, M. Takeyama, T. Matsuo. *Intermetallics* **10**, 915 (2002).

20. P. Feschotte, D. Lorin. *J. Less-Common Met.* **155**, 255 (1989).
21. W. C. Bragg, E. J. Williams. *Proc. R. Soc. London, Ser. A* **134**, 699 (1934).
22. W. C. Bragg, E. J. Williams. *Proc. R. Soc. London, Ser. A* **151**, 540 (1935).
23. C. Wagner, W. Schottky. *Z. Phys. Chem. B* **11**, 163 (1931).
24. G. G. Libowitz. In *Energetics in Metallurgical Phenomena*, Vol. 4, W. M. Mueller (Ed.), p. 71, Gordon and Breach, New York (1968).
25. R. Krachler, O. P. Semenova, H. Ipser. *Phys. Status Solidi B* **216**, 943 (1999).
26. S. B. Debiaggi, P. M. Decorte, A. M. Monti. *Phys. Status Solidi B* **195**, 37 (1996).
27. F. Gao, D. J. Bacon, G. J. Ackland. *Philos. Mag. A* **67**, 275 (1993).
28. S. M. Foiles, M. S. Daw. *J. Mater. Res.* **2**, 5 (1987).
29. C. L. Fu, G. S. Painter. *Acta Mater.* **45**, 481 (1997).
30. J. Sun, D. Lin. *Acta Metall. Mater.* **42**, 195 (1994).
31. H. Schweiger, E. Moroni, W. Wolf, W. Püschl, W. Pfeiler, R. Podloucky. *Mater. Res. Soc. Symp. Proc.* **552**, KK5.15.1 (1999).
32. H. Schweiger, O. Semenova, W. Wolf, W. Püschl, W. Pfeiler, R. Podloucky, H. Ipser. *Scripta Mater.* **46**, 37 (2002).
33. A. Steiner, K. L. Komarek. *Trans. Met. Soc. AIME* **230**, 786 (1964).
34. K. Hilpert, M. Miller, H. Gerads, H. Nickel. *Ber. Bunsen-Ges. Phys. Chem.* **94**, 40 (1990).
35. G. Kresse, J. Furthmüller. *Comput. Mater. Sci.* **15**, 6 (1996).
36. G. Kresse, J. Hafner. *J. Phys.: Condens. Matter* **6**, 8245 (1994).
37. W. Yuan, O. Diwald, A. Mikula, H. Ipser. *Z. Metallkd.* **91**, 448 (2000).
38. I. Katayama, S. Igi, Z. Kozuka. *Trans. JIM* **15**, 447 (1974).
39. A. Schweitzer, Y. Huang, W. Yuan, Z. Qiao, O. Semenova, F. Gehringer, H. Ipser. *Z. Naturforsch. B: Chem. Sci.* **59**, 999 (2004).
40. A. Schweitzer, X. Wu, W. Yuan, Y. Huang, J. Dischinger, H.-J. Schaller, Z. Qiao, F. Gehringer, H. Ipser. *Intermetallics* **12**, 401 (2004).
41. J. N. Pratt, J. M. Bird. *J. Phase Equilibr.* **14**, 465 (1993).
42. A. Kushida, T. Ikeda, H. Numakura, M. Koiwa. *J. Jpn. Inst. Metals* **64**, 202 (2000).
43. O. Semenova, R. Krachler, H. Ipser. *Solid State Sci.* **4**, 1113 (2002).
44. (a) V. V. Samokhval, P. A. Poleshchuk, A. A. Vecher. *Zh. Fiz. Khim.* **45**, 2071 (1971); (b) V. V. Samokhval, P. A. Poleshchuk, A. A. Vecher. *Russ. J. Phys. Chem.* **45**, 1174 (1971).
45. R. G. Reddy, A. M. Yahya, L. Brewer. *J. Alloys Compd.* **321**, 223 (2001).
46. M. Eckert, L. Bencze, D. Kath, H. Nickel, K. Hilpert. *Ber. Bunsen-Ges. Phys. Chem.* **100**, 418 (1996).
47. R. Würschum, E. A. Kümmerle, K. Badura-Gergen, A. Seeger, Chr. Herzig, H.-E. Schaefer. *J. Appl. Phys.* **80**, 724 (1996).
48. Y. Shirai, T. Murakami, N. Ogawa, M. Yamaguchi. *Intermetallics* **4**, 31 (1996).
49. J. Rüsing, Chr. Herzig. *Intermetallics* **4**, 647 (1996).
50. J. Rüsing, Chr. Herzig. *Scripta Met. Mater.* **33**, 561 (1995).
51. Chr. Herzig, M. Friesel, D. Derdau, S. V. Divinski. *Intermetallics* **7**, 1141 (1999).
52. H. Ipser, O. Semenova, R. Krachler. *J. Alloys Compd.* **338**, 20 (2002).
53. O. Kubaschewski. *Iron-Binary Phase Diagrams*, p. 5, Springer Verlag, Berlin (1982).
54. M. Fähnle, B. Meyer, J. Mayer, J. S. Oehrens, G. Bester. *Mater. Res. Soc. Symp. Proc.* **527**, 23 (1998).
55. Y. Huang, W. Yuan, Z. Qiao, O. Semenova, G. Bester, H. Ipser. *J. Alloys Compd.* **4**, 208 (2007).
56. B. Predel. *Landolt-Börnstein—Group IV: Physical Chemistry, Phase Equilibria, Crystallographic and Thermodynamic Data of Binary Alloys*, Vol. 5, Subvol. A, p. 244, Springer, Heidelberg (1991).
57. P. Feschotte, D. Lorin. *J. Less-Common Met.* **155**, 255 (1989).
58. S. Heinrich, H. U. Rexer, K. Schubert. *J. Less-Common Met.* **60**, 65 (1978).

59. O. G. Randl, G. Vogl, M. Kaisermayr, W. Bührer, J. Pannetier, W. Petry. *J. Phys.: Condens. Matter* **8**, 7689 (1996).
60. T. Heumann, H. Stüer. *Phys. Status Solidi* **15**, 95 (1966).
61. B. Sepiol, G. Vogl. *Phys. Rev. Lett.* **71**, 731 (1993).
62. B. Sepiol, O. G. Randl, C. Karner, A. Heiming, G. Vogl. *J. Phys.: Condens. Matter* **6**, L43 (1994).
63. G. Vogl, M. Kaisermayr, O. G. Randl. *J. Phys.: Condens. Matter* **8**, 4727 (1996).
64. G. Bester, B. Meyer, M. Fähnle. *Phys. Rev. B* **57**, R11019 (1998).
65. M. Fähnle, L. Schimmele. *Z. Metallkd.* **95**, 864 (2004).
66. A. Popovic, O. Semenova, K. W. Richter, R. Krachler, G. Bester, H. Ipser. *Intermetallics* **15**, 862 (2007).
67. O. Ikeda, I. Ohnuma, R. Kainuma, K. Ishida. *Intermetallics* **9**, 755 (2001).